Aerodynamic Optimization of Transonic High-Pressure Turbine Vanes with Non-Axisymmetric Endwalls for Rotating Detonation Engines

International Journal of Turbomachinery Propulsion and Power

Article

Aerodynamic Optimization of Transonic High-Pressure Turbine Vanes with Non-Axisymmetric Endwalls for Rotating Detonation Engines

Panagiotis Gallis [1], Sergio Grasa [2], Guillermo Paniagua [2], Simone Salvadori [1,*] and Daniela Anna Misul [1]

1 Department of Energy, Politecnico di Torino, Corso Duca degli Abruzzi 24, 10129 Torino, Italy; panagiotis.gallis@polito.it (P.G.); daniela.misul@polito.it (D.A.M.)
2 Zucrow Laboratories, Purdue University, 500 Allison Road, West Lafayette, IN 47907, USA; sgrasama@purdue.edu (S.G.); gpaniagua@me.com (G.P.)
* Correspondence: simone.salvadori@polito.it; Tel.: +39-0110904440

Abstract

For coupling a transonic high-pressure turbine vane with a rotating detonation combustor, several integration approaches have been considered. Endwall diffusion in the vane row can facilitate coupling by enabling a higher turbine inlet Mach number operating range. Nonetheless, the introduction of diffusive axisymmetric endwalls may promote flow separation and enlarged secondary flows, leading to an overall reduction in turbine stage efficiency. To address this, the present study introduces a shape optimization framework based on computational fluid dynamics for designing diffusive non-axisymmetric endwalls in a transonic vane downstream of a rotating detonation combustor. The reference geometry is a transonic vane with diffusive axisymmetric endwalls, previously analyzed in numerical studies. Both hub and shroud endwalls are parameterized using 20 design variables, and a random sampling approach generates 1000 distinct geometrical configurations. Each design undergoes geometry generation, meshing, and steady Reynolds-averaged Navier–Stokes computation under transonic conditions using a three-dimensional commercial solver. Aerodynamic performances are assessed, and a genetic aggregation method is employed to construct a response surface. A gradient-based optimization algorithm identifies the optimal non-axisymmetric endwall configuration, which is then simulated. Comparative analysis shows that the optimized non-axisymmetric endwall significantly mitigates hub and shroud vortex effects, enhancing aerodynamic efficiency and supporting integration within turbine systems equipped with rotating detonation combustors.

Keywords: pressure gain combustion; rotating detonation engine; computational fluid dynamics; shape optimization; non-axisymmetric endwalls

Check for updates

Academic Editor: Marcello Manna

Received: 2 April 2026
Revised: 20 May 2026
Accepted: 4 June 2026
Published: 12 August 2026

1. Introduction

Pressure gain combustion technologies offer significant power density and fuel burn improvement potential for gas turbines. In particular, rotating detonation combustors stand out given their annular chamber configuration and the lack of moving parts [1,2]. In these systems, detonative combustion raises the stagnation properties of the medium, theoretically leading to cycle efficiency enhancements, especially at low overall pressure ratios [3]. However, the high-frequency (1–10 kHz) circumferential motion of the detonation wave produces an inherently unsteady flow field with strong temporal and spatial oscillations [4,5].

The sensitivity of the combustor outflow to the geometry and to the boundary conditions [6,7] has led to a wide range of detonation modes and flow regimes over the operating envelope. This has motivated various integration approaches for coupling a rotating detonation combustor with a high-pressure turbine stage within a gas turbine system. The first is direct coupling with a supersonic turbine stage [8–10], avoiding pressure losses caused by the deceleration of the flow. However, strong shock reflections degrade aerodynamic performance, and advanced cooling schemes must fit within the limited supersonic vane space. Alternatively, a transition duct can partially decelerate the flow to suit a transonic vane [11], but it cannot reduce the Mach number to the typical inlet value (∼0.15) without causing significant losses. Therefore, axisymmetric diffusive endwalls upstream of the vane leading edge are necessary to further reduce the contraction ratio (increasing the inlet Mach number), thus ensuring the proper aerodynamic starting of the vane [12,13].

However, highly diffusive endwalls enlarge the cascade's secondary flows, as shown by several numerical studies [14–17]. Considering the rotating detonation combustor exhaust unsteadiness, these secondary flows oscillate strongly. A previous numerical study proposed an innovative flow control system to suppress their motion [16]. Despite the effectiveness of this technique in reducing their size, the hub and shroud passage vortices remain enlarged and significantly larger than those in traditional transonic high-pressure vanes with straight axisymmetric endwalls. As a result, non-axisymmetric endwall (NAE) contouring is explored to improve vane aerodynamic performance and reduce the size of secondary flows.

The non-axisymmetric endwall concept in turbomachinery originated from the need to reduce coolant supply pressure near the cavity of a high-pressure turbine stage. Rose et al. [18] proposed a non-axisymmetric endwall design for the vane hub to reduce pressure non-uniformities close to the cavity, creating "wavy" hub endwalls using axial curves with circumferential extrusion. Numerical simulations showed a 70% reduction in pressure non-uniformities, allowing for a lower coolant inlet pressure level. Their research extended to the Durham linear cascade through numerical and experimental studies [19], confirming improved flow guidance and reduced pressure non-uniformities. Further tests [20] showed a significant reduction in passage vortex size versus flat endwalls. Brennan et al. [20,21] applied non-axisymmetric endwalls to the hubs and shrouds of the Trent 500 turbine stages and used steady and unsteady simulations validated by experiments. Reduced secondary flows were observed at vane and blade outlets, with tests at varying speeds demonstrating non-axisymmetric endwall benefits over a wide operational range.

Later, Praisner et al. [22] applied hub non-axisymmetric endwalls to a Pratt and Whitney high-lift airfoil using gradient-based optimization, achieving a 25% loss reduction. Turgut et al. [23] created eight hub non-axisymmetric endwall profiles for a high-pressure turbine stage using a three-term Fourier series to generate sinusoidal shapes at different axial locations, reporting a 3.21% total pressure loss reduction under steady conditions for the best profile. Another numerical and experimental study on non-axisymmetric endwalls for both the hub and shroud of a vane showed total pressure loss reductions of 27% and 37%, respectively [24]. Moreover, the vane became aft-loaded, while the benefits were linked to the convex leading-edge region. A different optimization process on hub and shroud non-axisymmetric endwalls reduced vane total pressure losses by 3.79% [25], but no overall stage improvement occurred as the vane outlet flow angle was not included in the objective function.

Kim et al. [26] used response surface optimization to design non-axisymmetric endwalls at the hub or shroud of a high-pressure vane, achieving 8.5% total pressure loss reduction. Snedden et al. [27] studied non-axisymmetric endwalls on the vane hub of the one-and-a-half axial Durham turbine stage, concluding that it improved blade and stage efficiency and reduced secondary flow losses. Dickels et al. [28] applied hub non-axisymmetric endwalls on a linear high-lift airfoil, reporting 7.8% loss reduction from numerical simulations and experiments. Rheman et al. [29,30] used three-dimensional shape optimization with artificial neural networks for the hubs and shrouds of high-pressure vane, blade hub, and combined cases, achieving a 0.18% performance improvement and reduced vane and blade passage vortices. A case where solely non-axisymmetric endwall shroud optimization on the high-pressure vane was performed [31] yielded a 10.67% loss reduction. Finally, Burigana et al. [32] optimized non-axisymmetric endwalls on a blade hub with 3500 design of experiments (DOE) samples, achieving 0.3% stage efficiency gain.

In general, the application of non-axisymmetric endwalls on the turbine stages is an effective technique to reduce the size of hub and shroud passage vortices, leading to improved stage performance. The placement of a convex region accelerates the flow (decreasing pressure), whereas a concave region decelerates the flow (increasing pressure). Thus, the proper combination of convex and concave zones within the high-pressure vane passage can balance the pressure difference of the low-momentum fluid between the endwall suction side and pressure side, resulting in less intense secondary flows. Under this prism, the non-axisymmetric endwall technique is applied to the high-pressure vane with diffusive axisymmetric endwalls designed for coupling with a rotating detonation combustor [16]. This vane resulted from a prior numerical-based shape optimization process, which used the transonic CT3 vane with straight axisymmetric endwalls as the baseline case [33–35]. The current analysis uses the point-displacement method [22] to parameterize the hub and shroud surfaces of the vane. Then, a large design of experiments is created and evaluated through steady simulations. Finally, response surface optimization is employed to find the optimum design in terms of the kinetic loss coefficient, whose performance is thoroughly described and compared with the baseline axisymmetric endwall case and the best design of experiments sample.

To the authors' knowledge, this is the first study to optimize non-axisymmetric hub and shroud endwalls specifically for a transonic high-pressure turbine vane with highly diffusive endwalls intended for coupling with a rotating detonation combustor, providing a practically relevant design route for turbine designers to recover aerodynamic performance under this unconventional inlet environment.

2. Design Methodology

2.1. Optimization Strategy

The methodology that is adopted to implement the non-axisymmetric endwall concept on the high-pressure vane with diffusive axisymmetric endwalls includes shape optimization techniques. In Figure 1, the flow chart of the optimization strategy is displayed. The design strategy is split into three steps. First, the generation of geometries (Section 2.2) is conducted (A. Geometries in Figure 1). The axisymmetric endwalls are the baseline case, whose hub and shroud endwalls are parameterized with the help of b-spline curves. With the help of a random sampling method (namely a Sobol sequence), a design of experiments populated by a large pool of samples characterized by different non-axisymmetric endwall shapes is created. This part of the design process is thoroughly described in Section 2.3.

Once the geometries are generated, the performance of all samples must be assessed (B. Solver in Figure 1). Therefore, steady simulations are conducted. Each sample is first meshed, and appropriate boundary conditions are applied to the fluid domain to ensure the achievement of a transonic regime. These steps are included in Section 2.4. After the numerical assessment of every geometry, the sample evaluation is followed in Section 2.5.

Different metrics that specify the aerodynamic performance of the design of experiments vanes are introduced.

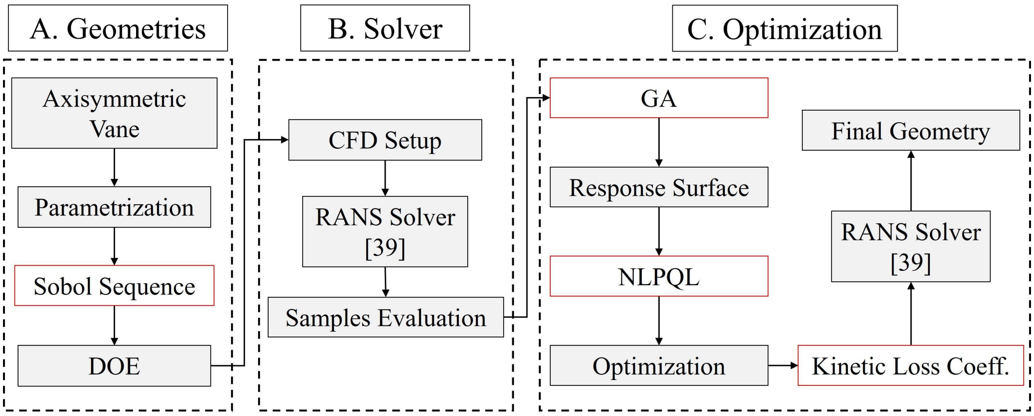

Figure 1. Flow chart of the design optimization process of diffusive non-axisymmetric endwalls for the high-pressure vane.

Finally, the design methodology is enclosed with the optimization part (C. Optimization in Figure 1) found in Section 3. After collecting all the evaluation data of the samples, an interpolation method is used to create a response surface that describes the relationship between the geometric parameters and the vane performance results. Then, a single-objective optimization of the response surface is conducted targeting the minimization of losses through the cascade. For that purpose, a gradient-based algorithm is used. Once the algorithm gives the prediction, the design is applied on the high-pressure vane, the meshed flow volume is created with the appropriate boundary conditions and its aerodynamic performance is numerical assessed. In the end, Section 4 presents a comparative study of the benefits provided by the final geometry, while Section 5 draws some conclusions from this research activity.

2.2. Geometry Generation

The baseline case of this analysis is the high-pressure vane with diffusive axisymmetric endwalls [16], which is displayed in Figure 2. Its major geometrical features are listed in Table 1 also. In this case, the inlet-to-outlet span ratio (SR) is 0.34, which results in significant diffusion in the meridional direction. The application of non-axisymmetric endwalls takes place on both hub and shroud. In Figure 3a, the blade-to-blade view of the cascade is shown. The vane passage is split into 4 axial (Z-axis) splines. Each spline is constructed with the help of 11 fit points. However, the first three and last three fit points are fixed in space, preserving tangency of the curve for the inlet and outlet flat endwalls. Upstream and downstream of the parameterized vane along the circumferential axis (X-axis), the parameterized pattern is identically repeated. The fit points are periodically duplicated to different azimuthal locations to ensure the proper repetition of the non-axisymmetric endwall shape. It is very important to ensure that the non-axisymmetric endwalls and the vane airfoil have the same spatial periodicity in the azimuthal direction [32]. Moreover, this approach allows for constructing smooth periodic surfaces in the azimuthal direction (X-axis), avoiding any presence of sharp edges at the locations of repetitions. In parallel, the parameterization is portrayed in meridional view of Figure 3b as well. The exact same parameterization occurs for both hub and shroud. The fit points have only one degree of freedom in radial direction (Y-axis). To construct a sample, first the variable fit points of hub are placed in the appropriate radial position. Then, the corresponding shroud fit points are mirrored by the hub fit points with respect to the mid-span of the cascade. Thus, a sample can be reconstructed with 20 fit points in total.

Table 1. Geometrical features of high-pressure vane with diffusive endwalls.

C	$C_{ax.}$	N_{Vanes}	$R_{Mid.}$	Sp_{In}	SR	$\alpha_{2,metal}$	CR
75.7 mm	51.67 mm	43	369.85 mm	17.2 mm	0.34	73 deg	1.24

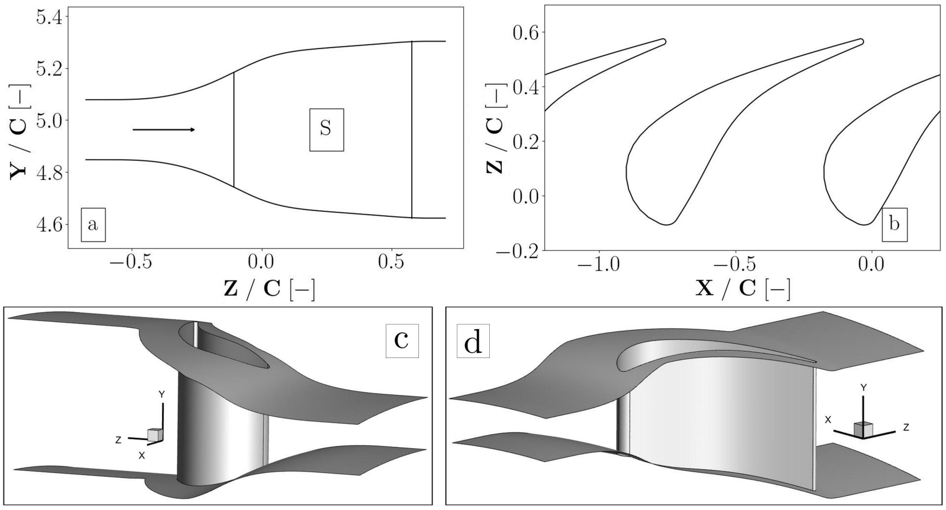

Figure 2. Meridional view (**a**), blade-to-blade view (**b**), iso-view 1 (**c**) and iso-view 2 (**d**) of the high-pressure vane with diffusive endwalls.

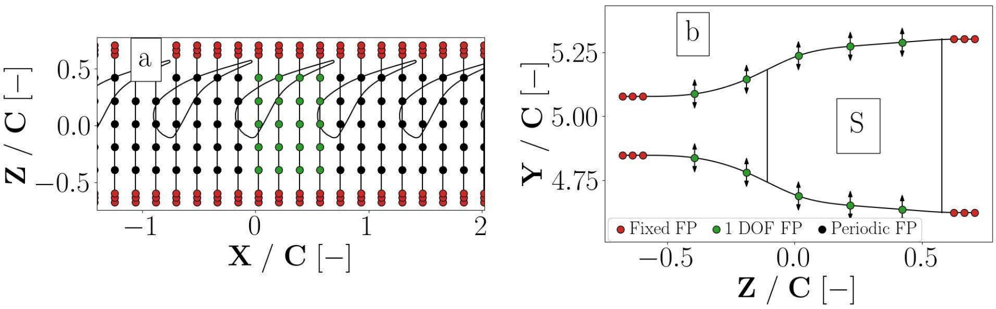

Figure 3. Parameterization of non-axisymmetric endwalls for the high-pressure vane shown in blade-to-blade view (**a**) and meridional view (**b**).

In Figure 4, a random sample is shown for its blade-to-blade view (a) and its meridional view (b). It is evident that the non-axisymmetric endwall configuration preserves the diffusivity characteristic, as shown in Figure 4a. Therefore, the un-starting phenomenon will be absent for that case and the inlet Mach number will remain high. It is demonstrated that the parameterized non-axisymmetric endwall shape inside of the central vane's passage ($0.018 - 0.57\ X/C$) is identically repeated for the next and previous vane passages respecting the spatial periodicity of the cascade, while it is easy to observe the mirror effect of shroud and hub axial splines in Figure 4b. In addition, the inlet area remains unchanged. Nonetheless, the non-axisymmetric endwall concept affects the throat area of the cascade. In order to ensure that the contraction ratio will not significantly vary for the design of experiments, the radial displacement of the fit points is restricted to $\pm 7.5\%$ of the corresponding axial span of the vane. Considering that a movement of a fit point occurs both in hub and shroud, the span variation for every axial location is permitted in range $\pm 15\%$. It is worth mentioning that these limits are in accordance with the evidence presented in the literature [36].

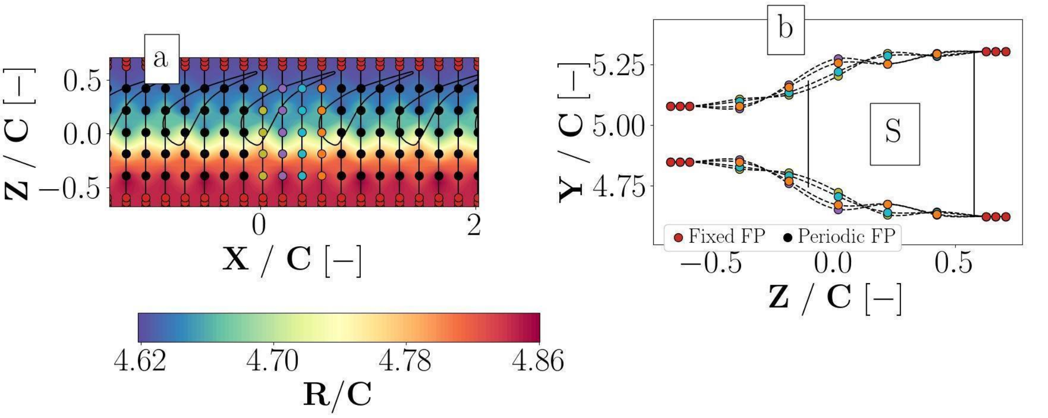

Figure 4. Random sample of non-axisymmetric endwalls for the high-pressure vane shown in blade-to-blade view (**a**) and meridional view (**b**).

2.3. Design of Experiments

Once the parameterization and the limits of the design of experiments are properly defined, its sampling process follows. The 4 axial stations along the vane pitch, each defined with 5 variable control points at both hub and shroud, result in a total of 20 design variables, as shown in Figure 3. These 20 variables constitute the input parameter space of the design of experiments (DOE). A space-filling random sampling method is then applied to these variables to generate 1000 unique design samples, each corresponding to a different combination of the input parameters. The DOE size of 1000 samples is selected considering the relatively high dimensionality of the design space (20 variables) and based on common practice reported in the literature, where comparable or smaller DOE sizes are typically adopted for similar optimization problems under computational constraints.

Thus, it is essential to carefully select this space-filling random sampling method to ensure consistent coverage of the design space. In statistics, the effective random sampling methods are characterized as low-discrepancy models. The metric called "discrepancy" quantifies the uniformity of the design points within the design space. In particular, the star discrepancy $\mathcal{D}^*$ is the maximum discrepancy value of a dataset and represents how well the design points are scattered in the design space. Methods with low values of $\mathcal{D}^*$ distribute the design points more uniformly in the design space without placing points very close or very far away from each other. More information regarding the discrepancy methods and assessments can be found in the works of Niederreiter [37] and Dalal et al. [38].

For the current analysis, three random sampling methods are compared, namely Sobol sequence, Halton sequence, and Latin hypercube. In Table 2, a parametric analysis of these three methods is given. It is evident that, for the needs of the current analysis, the Sobol sequence method provides the lowest discrepancy, ensuring a proper and uniform distribution of the design points in the multi-dimensional design space. Furthermore, Figure 5a gives a representation of the average percentage span variation of the vane for each sample. Since the cascade has diffusive endwalls and the NAE configuration imposes random displacement of the span, the average span percentage displacement along the vane's passage is necessary to be computed according to Equation (1). As a matter of fact, for every pitch-wise station (θ_i) of the parameterization, the span distribution along the axis ($Sp(Z, \theta_i)$) is compared with the nominal span distribution of axisymmetric endwall design ($Sp_{AE}(Z)$). Moreover, Figure 5b gives a graphical representation of the design of experiments limits in the meridional view of the high-pressure vane.

Table 2. Star discrepancy values for Sobol sequence, Halton sequence, and Latin hypercube for a design of experiments of 20 design parameters for 1000 samples.

$(\mathcal{D}^*)^{Sobol}_{Sequence}$	$(\mathcal{D}^*)^{Halton}_{Sequence}$	$(\mathcal{D}^*)^{Latin}_{Hypercube}$
0.0455	0.0496	0.0681

$$\overline{\Delta S_p} = \frac{1}{4}\sum_{i=1}^{4}\int_0^{Z_{TE}} \frac{Sp(Z,\theta_i) - Sp_{AE}(Z)}{Sp_{AE}(Z)}\,dZ \tag{1}$$

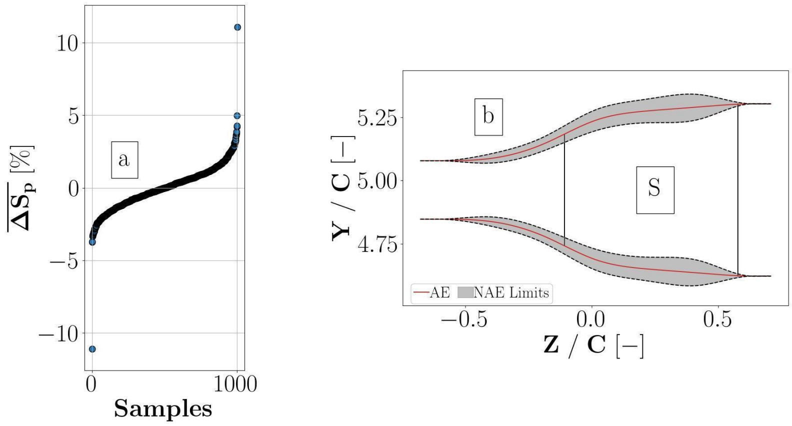

Figure 5. Percentage change of average span of the design of experiments non-axisymmetric endwall samples with respect to the axisymmetric endwall case (**a**) and geometrical variation of non-axisymmetric endwalls for the design of experiments presented in the meridional view (**b**).

2.4. Numerical Approach

Once the non-axisymmetric endwall samples for the design of experiments are properly designed, the numerical solving process follows (B in Figure 1). In Figure 6, the meshed volume domain of a random sample is given. The colors in Figure 6 correspond to the boundary conditions reported in Table 3. The boundary conditions are identical to those used for the vane with diffusive endwalls designed in [16], as well as the nominal conditions of CT3 vane [33–35] targeting the transonic regime of the cascade. Since no detailed information was available about inlet turbulence level and length scale, values of $Tu_{In} = 5\%$ and $Sc_{In} = 0.001$ m, which approximately correspond to 2.3% of the axial chord of the CT3 vane, were selected as representative of the test case. It must be underlined that the inlet length of the domain is chosen to allow for 5% growth of boundary layer with respect to the inlet span, ensuring that a developed flow will reach the cascade [14,15]. Moreover, the outlet sampling location is set at 0.3 of axial chord downstream of the trailing edge. The fine-meshed volume includes this location as well. As illustrated in Figure 6a, a large outlet plenum with free–slip walls is placed downstream of the cascade domain. The change in non-axisymmetric endwalls significantly varies the secondary flow development. Thus, the plenum ensures proper mixing of these vortical structures before reaching the outlet boundary and imposing difficulties on the calculations. In Figure 6d, it can be observed that inflation of 15 prismatic layers is placed on the walls of the domain, ensuring that y^+ will remain below unity, properly resolving the boundary layer.

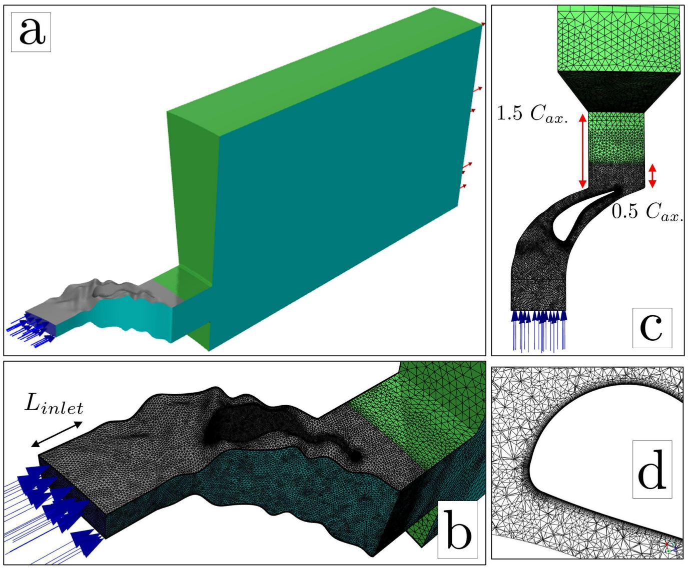

Figure 6. Iso-view of random non-axisymmetric endwall sample's domain (**a**), iso-view of meshed volume (**b**), blade-to-blade view of meshed volume (**c**) and detailed view of leading-edge mesh (**d**).

Table 3. Boundary conditions of cascade with non-axisymmetric endwalls.

Boundary Conditions	
Type	Properties
Inlet	P_t = 161,600 [Pa] & T_t = 440 [K]
Outlet	P = 83,289 [Pa]
Periodic	-
Free-Slip Wall	Adiabatic
No-Slip Wall	Adiabatic

After meshing every sample of the design of experiments, the steady three-dimensional calculations are performed for each case. The fully 2nd-order accurate density-based implicit commercial solver ANSYS™ FLUENT™ [39] version 2023R2 is used. The turbulence closure problem is treated with the help of k–ω SST turbulence model [40]. The hybrid mesh of each sample is around $2.4 \cdot 10^6$ elements. A grid-dependence analysis, as suggested by Roache et al. [41], is performed. For this purpose, two additional grids are tested with respect to the nominal (medium) one labeled as "M": a coarse grid (C) with $\approx 1.7 \cdot 10^6$ elements and a fine grid (F) with $\approx 3.1 \cdot 10^6$ elements. In Table 4, the results of the grid-dependence analysis are presented. The properties of vane inlet mass flow rate, vane inlet mass-weighted Mach number, and vane outlet mass-weighted total pressure are sampled for the three different grids. The GCI reduces from coarse–medium to medium–fine, while the asymptotic range of convergence is almost unity for all three properties. Thus, it is concluded that the numerical setup leads to grid-independent results.

Table 4. Grid dependence analysis of non-axisymmetric endwall high-pressure vane domain.

Property	Grid	Refinement Ratio	GCI	Asymptotic Range of Convergence
$(\dot{m})_{Inlet}^{Vane}$	C–M M–F	1.4 1.3	0.33% 0.18%	0.998

Table 4. *Cont.*

Property	Grid	Refinement Ratio	GCI	Asymptotic Range of Convergence
$(Ma)_{Inlet}^{Vane}$	C–M M–F	1.4 1.3	0.63% 0.38%	0.997
$(P_t)_{Outlet}^{Vane}$	C–M M–F	1.4 1.3	0.16% 0.19%	0.999

2.5. Vane Performance Evaluation

Once each sample's geometry is properly defined, meshed, and solved using a Reynolds-averaged Navier–Stokes solver, performance is subsequently evaluated. First of all, the peculiarity of the vane with diffusive endwalls lies in its low contraction ratio (associated with a high inlet Mach number), as defined in Equation (2). In spite of preserving the same inlet area (A_{in}) for all samples, the variation in endwall shape along the cascade alters the throat area (A^*) of the samples, which is calculated based on mass conservation.

$$CR = \frac{A_{in}}{A^*} \tag{2}$$

Concerning the aerodynamic performance of the vanes, the kinetic loss coefficient (Equation (3)) uncovers the effectiveness of the vane to accelerate the incoming flow. Moreover, the outlet flow angle coefficient indicates how much the outflow angle deviates from the prescribed outlet metal angle of the vane (Equation (4)). In other words, this metric assesses the effectiveness of flow guidance through the cascade.

$$\zeta_v = 1 - \frac{(u_2)^2}{(u_{2,\,is.})^2} = 1 - \frac{1 - \left(\frac{P_2}{P_{t,\,2}}\right)^{\frac{\gamma-1}{\gamma}}}{1 - \left(\frac{P_2}{P_{t,\,1}}\right)^{\frac{\gamma-1}{\gamma}}} \tag{3}$$

$$\zeta_{\alpha^o} = 1 - \frac{\alpha_2}{\alpha_{2,\,metal}} \tag{4}$$

The evaluation of the generated total pressure losses (ζ_{P_t}) through the cascade is usually expressed by Equation (5). In addition, another estimate is associated with the available outlet kinetic energy through the total pressure loss coefficient (Y), as shown in Equation (6). It would be useful to identify the different contributions of losses. Thus, the loss breakdown analysis (Equation (7)) is carried out using the loss correlations proposed by Aungier [42]. The contributions of the profile losses (Y_p), the secondary losses (Y_s), the trailing-edge losses (Y_{te}), and the shock losses (Y_{sh}) are included for the case of a high-pressure vane. Since the span of the diffusive axisymmetric endwall and non-axisymmetric endwall cases varies along the cascade, the secondary flow coefficient (Y_s) cannot be estimated using empirical models as the commonly used secondary loss correlation [42] requires a constant vane span. Therefore, the contribution of losses due to secondary flows is determined by subtracting the known coefficients of other loss mechanisms from the computed total pressure loss coefficient. The formulas of the employed coefficients are presented in Appendix A, whereas additional details concerning the derivation of the correlations and their corresponding expressions are provided in the work of Aungier [42].

$$\zeta_{P_t} = \frac{P_{t,\,in} - P_t}{P_{t,\,in}} \tag{5}$$

$$Y = \frac{P_{t,\,1} - P_{t,\,2}}{P_{t,\,2} - P_2} \tag{6}$$

$$Y = Y_p + Y_s + Y_{te} + Y_{sh} \tag{7}$$

Finally, the normalized outlet standard deviation of static pressure (Equation (8)) is used to assess the non-uniformity of vane outlet flow field (2) before reaching the possible subsequent turbine blade row [14,15]. In fact, diffusive endwalls promote enhanced secondary flows, so the outflow non-uniformities are significant. Also, the highly unsteady inflow from the rotating detonation combustor may induce blade-forcing phenomena in the subsequent blade row, so it is essential to quantify pressure fluctuations through the $\hat{\sigma}(P_2)$ parameter.

$$\hat{\sigma}(P_2) = \frac{\sigma(P_2)}{P_{t,\,in}} \tag{8}$$

3. Optimization Results

After all the design of experiments samples are generated, meshed, solved through three-dimensional simulations, and appropriately evaluated, the optimization strategy follows (C in Figure 1). The applied methodology is adopted based on the outcome of a preceding optimization of the high-pressure vane with axisymmetric diffusive endwalls [16], which is the baseline case for this non-axisymmetric endwall design process (Figure 2 and Table 1). The analysis is a single-objective optimization focusing on the minimization of the kinetic loss coefficient (ζ_v of Equation (3)). The deviation coefficient (ζ_{α^o} of Equation (4)) is not included as an objective function since it is treated as a secondary performance indicator rather than a primary design target in the present formulation. The whole process is conducted with the help of ANSYS DesignXplorer version 2023R2 tool [43]. After collecting all the results of the design of experiments, the construction of the response surface occurs. The genetic aggregation method is used to interpolate and construct a response surface. The response surface is a function that receives as inputs the geometrical values of the design points (r_i) and returns the analyzed properties retrieved by the simulations (CR, ζ_v, ζ_{α^o}, Y, $\hat{\sigma}(P)$, etc.). It is an iterative process that is initialized by already defined interpolation methods (full second-order polynomials, non-parametric regression, Kriging, and moving least squares). Then, the processes of selection, crossover and mutation are followed. The genetic aggregation method continues for 12 iteration, while a stopping criterion with respect to the goodness of fit evaluation is integrated.

In Figure 7, a three-dimensional representation of the response surface is displayed. The kinetic loss coefficient (ζ_v) is shown with respect to the design parameters r_4 and r_8. In particular, r_4 is the first variable fit point of 0.018 X/C axial spline in Figure 3, which is the first axial spline downstream of the leading edge in the pitch-wise direction (X-axis). For the same spline, r_8 is the fifth variable fit point. In parallel, the surface is colored with the values of deviation coefficient (ζ_{α^o}). Since the design parameters are 20, it is impossible to visualize the response surface for the kinetic loss coefficient for all the design parameters. This is the reason why the representation with only two design parameters is selected. The response surface representation of Figure 7 can be extended to all the combinations of the 20 design parameters of the design of experiments. The quality of the response surface interpolation by genetic aggregation is given in Figure 8. In this diagram, the non-dimensional observed values by the design of experiments for all the samples regarding the kinetic loss coefficient, deviation coefficient, and contraction ratio are placed in the x-axis, whereas the y-axis represents the predicted values by the response surface for the corresponding properties. In parallel, the coefficient of determination (R^2) is computed for the three aforementioned properties. It is evident that the R^2 does not drop below 99.7%

for the three cases, denoting the successful interpolation and construction of the response surface by the genetic aggregation method.

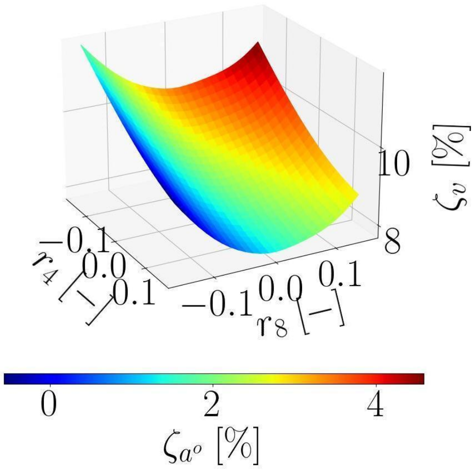

Figure 7. 3D representation of response surface for r_4 and r_8 design parameters with respect to the kinetic loss coefficient (ζ_v) colored with values of deviation coefficient (ζ_{α^o}).

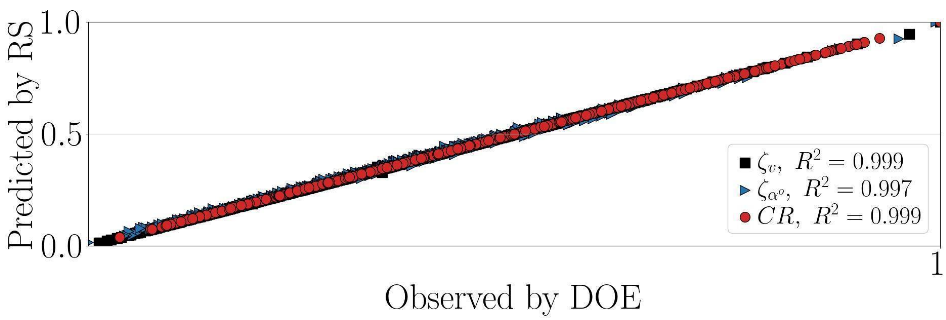

Figure 8. Quality of response surface interpolation measured for kinetic loss coefficient (ζ_v), deviation coefficient (ζ_{α^o}) and contraction ratio (CR) of non-axisymmetric endwall design of experiments samples.

Once the response surface is constructed and its quality is evaluated, the optimization of the response surface is followed. For that purpose, the non-linear programming by quadratic Lagrangian (NLPQL) method is used. It is a gradient-based single-objective optimizer based on quasi-Newton methods. It is an iterative process that stops when the two subsequent predictions of the objective function (ζ_v) do not change more than 0.0001%. Once the optimizer provides a candidate, the elected sample is designed, meshed, and solved in order to validate the prediction. If the validation is worse than the best sample of the design of experiments, the sample is added to it and the optimization process (C in Figure 1) repeats. If the optimized validation shows improvement, the final design of non-axisymmetric endwalls is created. More information regarding the response surface construction and optimization can be found in [43].

4. Turbine Vane Analysis

In Figure 9, the results of the design of experiments are presented. The x-axis is the deviation coefficient (ζ_{α^o} of Equation (4)), while the y-axis is the kinetic loss coefficient (ζ_v of Equation (3)). Its minimization constitutes the single-objective function of the optimization process. Moreover, in Figure 9a, the samples are colored with the contraction ratio (CR of Equation (2)), whereas, in Figure 9b, the cases are colored with the non-dimensional outlet standard deviation of pressure ($\hat{\sigma}(P_2)$ of Equation (8)). In addition, for both graphs, different symbols highlight the baseline axisymmetric endwalls (AEs), the non-axisymmetric endwall samples of the design of experiments (DOE NAEs), the sample of design of experiments with minimum combination of kinetic loss coefficient and deviation flow angle coefficient (DOE NAE), and the optimized sample (Opt. NAE). First of all, the success rate of the design of experiments process regarding design, meshing, and solving cases reaches 99.8% since only two cases fail during the process. Moreover, the candidate predicted by the NLPQL method showed a validated performance improvement over the best design of experiments sample, thereby eliminating the need for the optimizer to initiate an additional optimization round. In terms of kinetic loss coefficient, 7.4% of the design of experiments samples show improvement with respect to the baseline axisymmetric case, while the percentage for the deviation coefficient reaches 37.7%. Moreover, the optimized case shows an improvement of 23.43%, achieving the goal of the design process. The results of the optimization process are displayed in Table 5. In general, the optimized case accomplishes substantial improvement for all the assessment parameters except the minor better performance of $\hat{\sigma}(P_2)$. It must be reported that, for all the cases, the Reynolds number based on the chord of the vane is approximately $1 \cdot 10^6$, reaching an outlet Mach number of approximately 0.93.

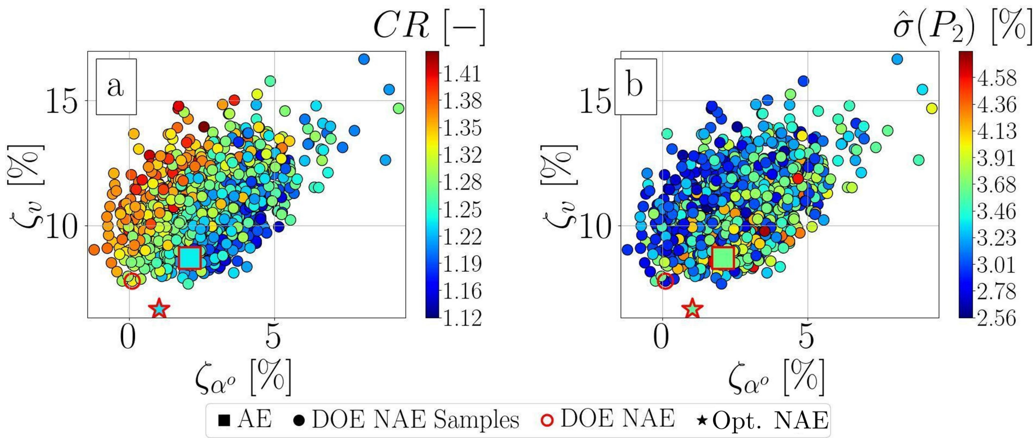

Figure 9. Non-axisymmetric endwall design of experiments and optimization results shown with respect to the contraction ratio (CR) (**a**) and non-dimensional outlet standard deviation of pressure ($\hat{\sigma}(P_2)$) (**b**).

Table 5. Performance comparison of axisymmetric endwalls (AEs), best by DOE non-axisymmetric endwalls (DOE NAEs) and optimized non-axisymmetric endwalls (Opt. NAEs).

Case	Ma_{in}	CR	ζ_v %	Y %	ζ_{α^o} %	$\hat{\sigma}(P_2)$ %
AE	0.57	1.24	8.7	14.07	2.1	3.65
DOE NAE	0.51	1.33	7.8	12.32	0.11	2.8
Opt. NAE	0.57	1.23	6.7	10.45	1	3.56
Net improvement	-	-	2	3.62	1.1	0.09

In Figure 9a, it is visible that an increased contraction ratio reduces the deviation coefficient, which is in accordance with the preceding optimization results of the high-pressure vane with axisymmetric diffusive endwalls [16]. A larger contraction ratio leads to a lower inlet Mach number for the cascade. Thus, the vane is able to turn the flow more efficiently since the receiving inlet velocity is lower. Regarding the kinetic loss coefficient, no clear regression with respect to the contraction ratio can be derived. In addition, non-axisymmetric endwalls do not exhibit major variations in non-dimensional outlet standard deviation of pressure, as shown in Figure 9b. However, a small improvement in pressure reduction regarding non-uniformities at the outlet is achieved. In conclusion, the optimized case of non-axisymmetric endwalls achieves reduced total pressure losses through the cascade, better guides the flow, and does not trigger significant outlet pressure non-uniformities regarding the blade-forcing phenomena for the possible subsequent blade row.

In Figure 10, the front and rear iso-views of the hub endwalls for the baseline axisymmetric endwall case, the best non-axisymmetric endwall case by design of experiments and the optimized non-axisymmetric endwall geometry are shown. Moreover, the hub endwalls are colored with respect to the non-dimensional radius. In Figure 10b,c, it is evident that, for the best by design of experiments non-axisymmetric endwall and optimized non-axisymmetric endwall cases, convex regions are placed at the location of leading edge. In particular, the leading-edge convex region is more intense for the optimized non-axisymmetric endwall, while an additional convex region is added at the middle of the entrance vane's passage. Downstream, it is displayed that the optimized non-axisymmetric endwall geometry exhibits a concave region close to the suction side, while a slight convex region is observed close to the pressure side. This is more evident in Figure 10f. Furthermore, in the rear view (Figure 10e), a sudden "bump" can be identified in the aft region of the suction side for the best non-axisymmetric endwall case obtained from the design of experiments (DOE NAEs). This convex region is much milder for the case of optimized non-axisymmetric endwalls.

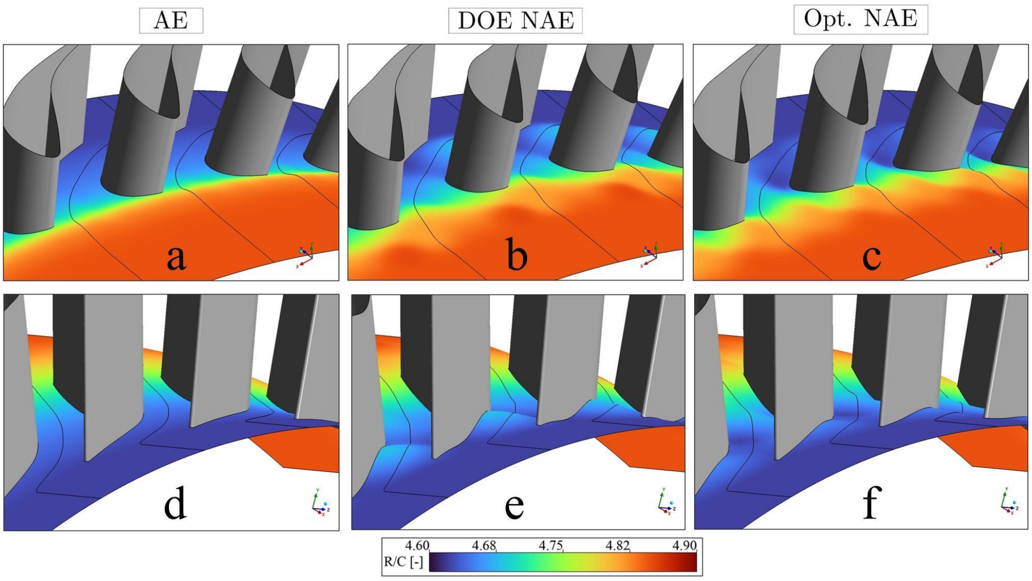

Figure 10. Iso-view for axisymmetric endwalls (AEs), best non-axisymmetric endwalls (NAEs) by DOE, and optimized non-axisymmetric endwalls: (**a**–**c**) front view; (**d**–**f**) rear view.

The Mach number contour at mid-span for the three cases is shown in Figure 11. It is evident that a strong shock is generated at the suction side of design of experiments non-axisymmetric endwalls. Nonetheless, this shock is moved downstream and is much milder for the optimized geometry. The presence of this sudden acceleration is accounted for by the presence of "bump" for the two non-axisymmetric endwall cases, as shown in Figure 10. This downstream convex region close to the suction side of the trailing edge contracts the flow field further, resulting in extra acceleration. However, the "bump" is less intense for the optimized non-axisymmetric endwalls, thus alleviating the effect of a strong shock.

The outlet pressure loss contours are presented in Figure 12. The axisymmetric endwall case has strong hub and shroud passage vortex cores (which are identified by considering the radial position of the highest pressure loss point) that are very close to the mid-span.

Their span penetration heights are 42.23 % and 68.2 %, respectively. These cores are much milder for the best by design of experiments non-axisymmetric endwall case and they are moved closer to the related endwalls, leading to span penetration heights equal to 28.75 % for the hub passage vortex and 86.54 % for the shroud passage vortex. Nonetheless, a strong hub corner vortex can be identified. Conversely, the optimized non-axisymmetric endwall case exhibits a much milder hub corner vortex, which is located closer to the hub endwalls. Similarly, the hub and shroud passage vortices are less intense and placed away from the mid-span, attaining span penetration heights equal to 32.17 % for the hub passage vortex and 78.23 % for the shroud passage vortex.

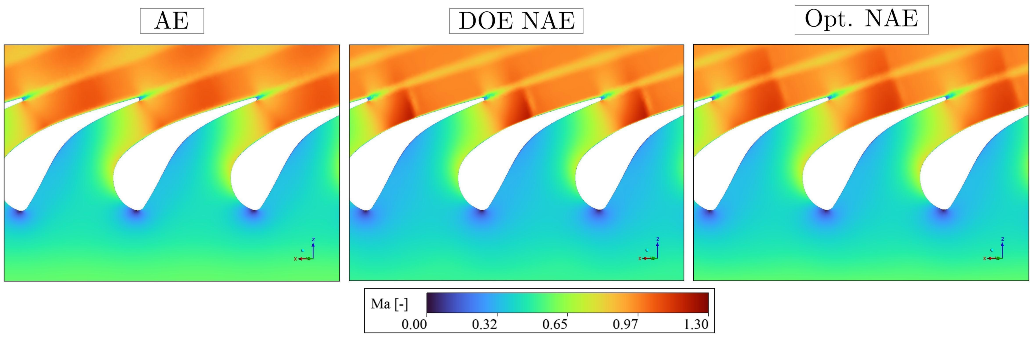

Figure 11. Mid-span contour Mach number for axisymmetric endwalls (AEs), best by DOE non-axisymmetric endwalls (DOE NAEs) and optimized non-axisymmetric endwalls (Opt. NAEs).

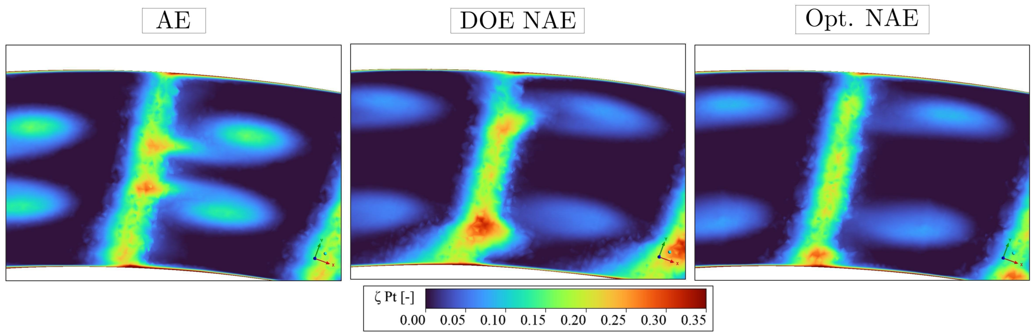

Figure 12. Outlet contour of total pressure losses for axisymmetric endwalls (AEs), best by DOE non-axisymmetric endwalls (DOE NAEs) and optimized non-axisymmetric endwalls (Opt. NAEs).

In Figure 13a, the isentropic Mach number distribution at mid-span for the three cases is displayed. As reported in the literature, the vane is transformed to more aft-loaded airfoil since the maximum acceleration occurs upstream for both the best by design of experiments non-axisymmetric endwalls and the optimized non-axisymmetric endwalls with respect to the axisymmetric endwall case. The best by design of experiments non-axisymmetric endwall sample exhibits a strong peak of $Ma_{is.}$, which is much milder for the optimized non-axisymmetric endwalls. In Figure 13b, the radial distribution of pitch-wise averaged total pressure losses for the three cases is shown. Both cases of non-axisymmetric endwalls push the core of passage vortices towards the hub and shroud, while the cores exhibit decreased losses. However, the passage vortex of best by design of experiments non-axisymmetric endwalls generates significant total pressure losses. In general, the optimized non-axisymmetric endwall case is an aft-loaded vane with mild acceleration of the suction side, while the hub and shroud passage vortices are less intense and closer to the related endwalls.

In addition, Figure 14 shows the radial distribution of pitch-wise averaged outlet yaw angle. Both non-axisymmetric endwall cases achieve less under-turning close to the mid-span region, confirming the deviation coefficient improvement shown in Figure 9.

Moreover, they exhibit less over-turning close to the shroud region. However, the best by design of experiments non-axisymmetric endwall case is characterized by excessive over-turning close to the hub endwall, evidence of the strong corner vortex shown in Figure 12. The absence of this intense rear bump for the optimized non-axisymmetric endwall case (Figure 10f) effectively restricts the over-turning in that region.

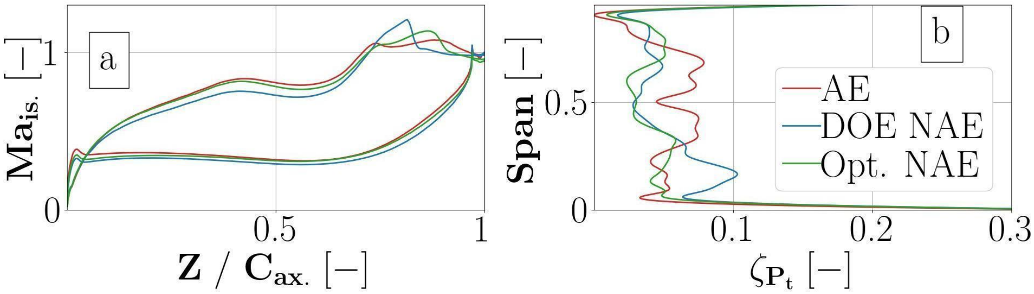

Figure 13. Isentropic Mach number distribution at mid-span (**a**) and outlet total pressure loss distribution (**b**) for axisymmetric endwalls (AEs), best by DOE non-axisymmetric endwalls (DOE NAEs) and optimized non-axisymmetric endwalls (Opt. NAEs).

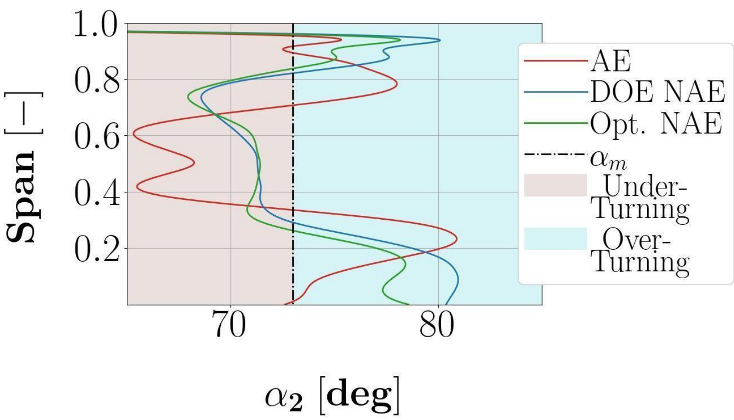

Figure 14. Outlet spanwise distribution of yaw angle for axisymmetric endwalls (AEs), best by DOE non-axisymmetric endwalls (DOE NAEs) and optimized non-axisymmetric endwalls (Opt. NAEs).

In Figure 15, the front and rear views of the hub secondary flows are displayed with the help of vorticity magnitude iso-surfaces ($|\omega_\zeta| \geq 2 \cdot 10^4\ 1/s$). The convex regions close to the leading edge for the non-axisymmetric endwall cases reduce the size of horseshoe vortices, as visible in Figure 15b,c. As a consequence, when the pressure side and suction side horseshoe vortices merge and form the hub passage vortex, its size is significantly smaller compared to the axisymmetric endwall case (see Figure 15a). Moreover, the concave regions close to the suction side for the non-axisymmetric endwall cases increase the pressure close to that zone. Thus, the hub passage vortex does not impinge on the suction side as in the axisymmetric endwall case. Therefore, the vortex is not further accelerated, restricting its intensity and size. On the other hand, the downstream "bump" close to the suction side of the trailing edge reported for the design of experiments non-axisymmetric endwall generates an intense hub corner vortex, as shown in Figure 15e. Nonetheless, the optimizer successfully detects this effect and the elected geometry reduces this convex region (as shown in Figure 10f), leading to a much milder hub corner vortex.

The non-dimensional pressure at the hub surface for the three cases is displayed in Figure 16. Starting from the inlet of the cascades, the axisymmetric endwall case shows a highly irregular hub endwall pressure distribution. The best by design of experiments non-axisymmetric endwall case demonstrates some improvement. However, regions of low pressure are still accompanied by adjacent high-pressure zones. A low-pressure ring surrounds the leading-edge region, followed by a pressure increase near the leading-edge stagnation point. In contrast, the optimized non-axisymmetric endwall case exhibits a uniform pressure rise from the inlet to the leading-edge stagnation point. A more uniform inlet pressure distribution results in less intense horseshoe vortex legs, leading to a weaker passage vortex.

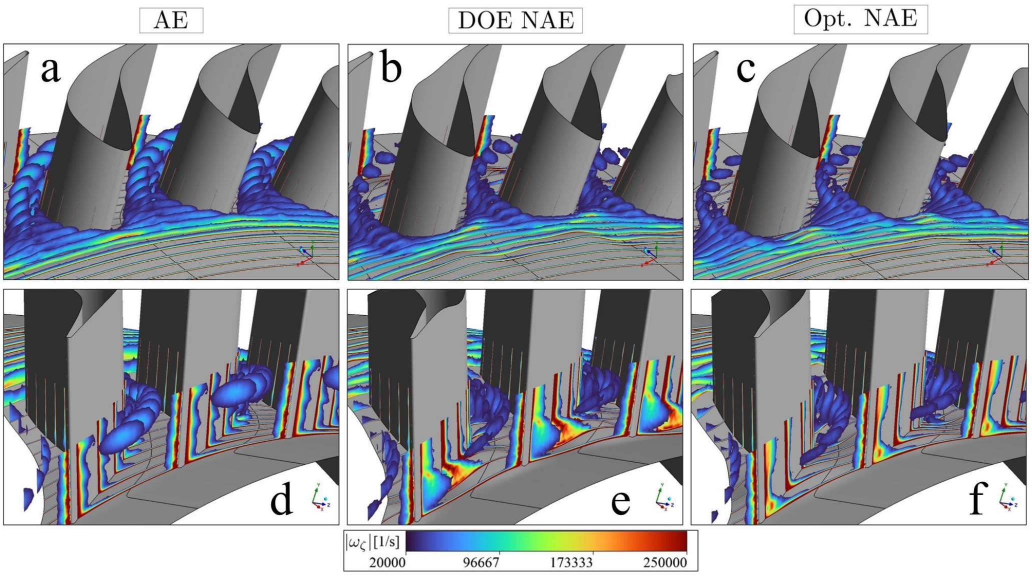

Figure 15. Iso-view of vorticity magnitude iso-surfaces for axisymmetric endwalls (AEs), best by DOE non-axisymmetric endwalls (DOE NAEs) and optimized non-axisymmetric endwalls (Opt. NAEs) (iso-surfaces of $|\omega_\zeta| \geq 2 \cdot 10^4\ 1/s$): (**a**–**c**) front view; (**d**–**f**) rear view.

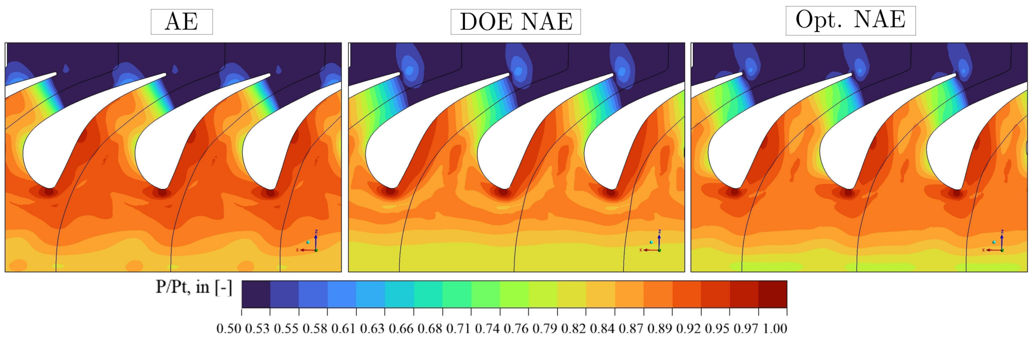

Figure 16. Blade-to-blade view of non-dimensional static pressure distribution at hub walls for axisymmetric endwalls (AEs), best by DOE non-axisymmetric endwalls (DOE NAEs) and optimized non-axisymmetric endwalls (Opt. NAEs).

In the aft part of the vanes, downstream of the suction side crest, the baseline geometry presents a strong circumferential pressure difference between the pressure side and suction side, which can be identified by the highly warped pressure iso-lines in that region. This pressure imbalance promotes the motion of the passage vortex from the pressure side to the suction side, contributing to the overall growth and radial penetration of the secondary flows [44]. Contrarily, the best design of experiments and optimized designs exhibit a more uniform circumferential pressure distribution, with pressure iso-lines parallel to the mid-pitch flow turning line, thereby minimizing the motion of the passage vortex towards the suction side. For the same location, it is evident that the expansion of low-momentum flow near the endwalls occurs much more smoothly in the non-axisymmetric endwall cases compared to the baseline axisymmetric endwall case. For all these reasons, the non-axisymmetric endwall application results in less intense secondary flows, reducing total pressure losses and improving flow guidance.

Finally, the loss budget breakdown analysis for the three cases is reported in Table 6. The profile losses are elevated for the non-axisymmetric endwall cases. Since the airfoil profile is not optimized for the non-axisymmetric endwall configuration but for the axisymmetric endwall case, it is clear that the contribution of losses by the airfoil shape is higher. For the trailing-edge losses, the three cases exhibit similar results. However, the shock losses are higher for the non-axisymmetric endwall cases, especially for the design of experiments non-axisymmetric endwalls. These results are in accordance with the remarks derived from the Mach number contour of mid-span (Figure 11) and the mid-span isentropic Mach number distribution (Figure 13a). The non-axisymmetric endwall cases augment the losses due to the presence of shock. However, the optimizer successfully subtracts these losses by alleviating the intensity of the shock. Finally, both non-axisymmetric endwall cases substantially reduce the contribution of secondary flow losses. The baseline axisymmetric endwall case reaches almost 8 % of Y_s, whereas the optimized non-axisymmetric endwalls do not exceed the limit of 3 %.

Table 6. Loss budget breakdown analysis for axisymmetric endwalls (AEs), best by DOE non-axisymmetric endwalls (DOE NAEs) and optimized non-axisymmetric endwalls (Opt. NAEs), including profile losses Y_p, trailing-edge losses Y_{TE}, shock losses Y_{sh} and secondary flow losses Y_s (d).

Case	Y %	Y_p %	Y_{te} %	Y_{sh} %	Y_s %
AE	14.08	5.48	0.72	0.13	7.75
DOE NAE	12.32	7.74	0.82	1.91	1.86
Opt. NAE	10.46	6.36	0.71	0.58	2.80
Net improvement	3.62	−0.38	0.01	−0.45	4.95

5. Conclusions

This research work describes the shape-based numerical design optimization of diffusive non-axisymmetric endwalls for a high-pressure turbine vane. The non-axisymmetric endwall concept has been demonstrated to effectively reduce the cascade's secondary flows, achieving more uniform outflow. Thus, this advanced technique is applied to the peculiar case of a high-pressure vane with diffusive endwalls, which can potentially be placed downstream of a rotating detonation combustor.

The baseline case of this study is the high-pressure vane with diffusive axisymmetric endwalls derived by a previously performed numerical work. The point-displacement parameterization of both hub and shroud endwalls is chosen, including 20 fit points that can move only in the radial direction. With the help of Sobol sequences, 1000 cases are generated. All the samples pass the design, mesh and numerical setup processes. Reynolds-averaged Navier–Stokes calculations are conducted in each case, and aerodynamic sample evaluation is followed. In the end, a response surface is constructed using genetic aggregation, while the non-linear programming by quadratic Lagrangian method, with the minimization of the kinetic loss coefficient as the single objective, identifies the optimum case.

The combination of concave and convex regions at the cascade endwalls can balance the pressure fluctuation of the low-momentum fluid in these regions. In fact, the optimum non-axisymmetric endwall case is characterized by a convex region close to the leading edge, while a similar zone is observed in the middle of the vane's entrance. In addition, a concave zone is placed close to the rear part of the suction side of the vane. A remarkable 23.43% kinetic loss coefficient reduction is achieved, while both the outlet pressure uniformities and flow guidance are improved as well. The non-axisymmetric endwall airfoils exhibit aft-loaded vane characteristics, confirming the findings reported in the literature. Additionally, a convex region near the rear portion of the suction side of the non-axisymmetric endwall airfoil further contracts the flow field, thereby increasing compressibility losses. Nevertheless, the contribution of secondary flows to the total pressure losses is significantly reduced.

Both hub and shroud passage vortices are less intense, resulting in higher-quality flow for the subsequent blade row. The non-axisymmetric endwall application effectively redirected secondary flows closer to the endwalls, reducing their impact near the outlet mid-span region. While diffusive endwalls are necessary for starting the vane, they were previously associated with enlarged hub and shroud passage vortices that significantly degrade overall stage performance. This new technique, however, overcomes that limitation and can be adopted for innovative transonic vanes potentially placed downstream of a rotating detonation combustor.

For turbine designers, these results demonstrate that non-axisymmetric endwall shaping is not only an original enabler for transonic vane architectures that are compatible with rotating detonation combustors but also a practical means to mitigate secondary flow penalties and deliver a more uniform higher-quality outflow for the downstream blade row.

Author Contributions: Conceptualization, P.G., S.G., G.P., S.S. and D.A.M.; software, P.G.; validation, P.G.; investigation, P.G.; resources, S.G. and G.P.; data curation, P.G.; writing—original draft preparation, P.G.; writing—review and editing, P.G. and S.S.; visualization, P.G.; supervision, G.P., S.S. and D.A.M. All authors have read and agreed to the published version of the manuscript.

Funding: The present activity was performed in the frame of the INSPIRE project (Grant Agreement 956803) funded by the European Commission through a Marie Sklodowska-Curie Action. This research was also supported in part by an appointment of Paniagua to the National Energy Technology Laboratory (NETL) through the NETL Faculty Research Program (FRP), sponsored by the U.S. Department of Energy and administered by ORISE.

Institutional Review Board Statement: Not applicable.

Data Availability Statement: The original contributions presented in this study are included in the article. Further inquiries can be directed to the corresponding author.

Conflicts of Interest: The authors declare no conflicts of interest.

Nomenclature

Roman Symbols

C	Chord [m]
N_vanes	Number of Vanes [−]
DR	Half Span [m]
$\mathcal{D}^*$	Star Discrepancy [−]
$\mathcal{D}$	Discrepancy [−]
GCI	Grid Convergence Index [−]
$\dot{m}$	Mass Flow Rate [kg/s]
Ma	Mach Number [−]
P_t	Total Pressure [Pa]
T_t	Total Temperature [K]
CR	Contraction Ratio [−]
A	Area [m^2]
A	Area [m^2]
ptc	Pitch [m]
o	Throat [m]
t_2	Trailing-Edge Thickness [m]
u	Velocity [m/s]

Sc	Turbulent Length Scale [m]
Sp	Span [m]
SR	Span Ratio $[-]$
Tu	Turbulence Level $[-]$
Y	Total Pressure Loss Coefficient [m/s]
$Y_c l$	Clearance Loss Coefficient $[-]$
$Y_e x$	Supersonic Expansion Loss Coefficient $[-]$
$Y_l w$	Lashing Wire Loss Coefficient $[-]$
Y_p	Profile Loss Coefficient $[-]$
Y_s	Secondary Flow Loss Coefficient $[-]$
$Y_t e$	Trailing-Edge Loss Coefficient $[-]$
$Y_s h$	Shock Loss Coefficient $[-]$
r	Design Parameter $[-]$
R^2	Coefficient of Determination $[-]$
R	Radius [m]
Greek Symbols	
ΔSp	Span Variation $[-]$
γ	Specific Heat Ratio $[-]$
α	Yaw Angle [deg]
β	Pitch Angle [deg]
ζ_v	Kinetic Loss Coefficient $[-]$
ζ_{P_t}	Total Pressure Losses $[-]$
ζ_{α^o}	Deviation Angle Coefficient $[-]$
$\hat{\sigma}(P)$	Normalized Outlet Standard Deviation of Static Pressure $[-]$
ω_ζ	Vorticity Magnitude $[\mathrm{s}^{-1}]$
Superscripts	
$Is.$	Isentropic
$ax.$	Axial
In	Inlet
Out	Outlet
$metal$	Metal Angle
Mid	Mid-Span

Abbreviations

The following abbreviations are used in this manuscript:

AE	Axisymmetric Endwall
CR	Contraction Ratio
DOE	Design of Experiments
DOE NAE	Best Sample from Design of Experiments
FP	Fit Point
NAE	Non-Axisymmetric Endwall
Opt. NAE	Optimized Sample
NLPQL	Non-Linear Programming by Quadratic Lagrangian
SR	Span Ratio

Appendix A

The total pressure loss coefficient evaluation is based on empirical performance correlations for axial-flow turbine blade and vane rows, as proposed by Aungier [42]. In this framework, the total pressure loss coefficient is expressed as the sum of the individual loss sources within the turbine stage, as shown in Equation (A1). For the present case, which focuses solely on the vane performance analysis, the contributions of losses due to leakage, supersonic expansion, and lashing wire are neglected, i.e., $Y_{cl} = Y_{ex} = Y_{lw} = 0$. The profile loss coefficient (Y_p) represents the losses caused by the boundary layers developing along the endwalls and airfoil surfaces, as well as those induced by the incidence at the cascade inlet. The secondary flow loss coefficient (Y_s) accounts for the losses generated by the influence of centrifugal forces within the passage flow. The trailing-edge term (Y_{te}) corresponds to the losses associated with the cascade wake, whereas the shock loss coefficient (Y_{sh}) reflects the compressibility effects occurring through the passage.

Most of the coefficients are calculated using the correlations proposed by Aungier [42], as shown in Table A1. The contribution of secondary losses (Y_s) cannot be determined using these correlations because the vane span varies along the axis, which violates the correlation's assumption of constant span. Since the total pressure loss coefficient (Y) of the cascade is calculated according to Equation (6) using numerical results, the remaining unknown coefficient representing the secondary flows is derived from Equation (A2). Further details regarding the derivation, definitions of the additional parameters, and relations required to compute each loss coefficient are provided in [42].

$$Y = Y_p + Y_s + Y_{te} + Y_{cl} + Y_{ex} + Y_{sh} + Y_{lw} \tag{A1}$$

$$Y_s = Y - (Y_p + Y_{te} + Y_{sh}) \tag{A2}$$

Table A1. Total pressure loss coefficients of a vane.

Profile Losses	$Y_p = K_{mod}K_{inc}K_M K_M K_P K_{RE} A$ $A = [Y_{p1} + \Xi(Y_{p2} - Y_{p1})](5 \cdot t_{max} / c)^{\Xi} - \Delta Y_{te}$ $\Xi = \alpha_{2,\ metal} / \alpha_2$
Trailing-Edge Losses	$Y_{te} = 2\, \Delta P_t / (\rho u^2)$ $\Delta P_t = \frac{1}{2}\rho u^2 [ptc \cdot sin\beta g / (ptc \cdot sin\beta g - t_2) - 1]^2$ $\beta g = arcsin(o / ptc)$
Shock Losses	$Y_{sh} = \sqrt{\tilde{Y}_{sh}^2 / (1 + \tilde{Y}_{sh}^2)}$ $\tilde{Y}_{sh} = 0.8 \cdot X_1^2 + X_2^2$ $X_1 = 0$, if $Ma_1 \leq 0.4$ $X_1 = Ma_1 - 0.4$, if $Ma_1 > 0.4$ $X_2 = 0$, if $Ma_1 \leq Ma_2$ $X_2 = Ma_1 / Ma_2 - 1$, if $Ma_1 > Ma_2$

References

1. Purushothaman, S.; Renuke, A.; Sorce, A.; Traverso, A. A Review of Pressure Gain Combustion Solutions for Aerospace Propulsion. In *Proceedings of the Volume 4: Cycle Innovations; Cycle Innovations: Energy Storage, Rotterdam, The Netherlands, 13–17 June 2022*; GT2022; American Society of Mechanical Engineers: New York, NY , USA, 2022. [CrossRef]
2. Ma, J.Z.; Luan, M.Y.; Xia, Z.J.; Wang, J.P.; Zhang, S.; Yao, S.; Wang, B. Recent Progress, Development Trends, and Consideration of Continuous Detonation Engines. *AIAA J.* **2020**, *58*, 4976–5035. [CrossRef]
3. Sousa, J.; Paniagua, G.; Collado Morata, E. Thermodynamic Analysis of a Gas Turbine Engine with a Rotating Detonation Combustor. *Appl. Energy* **2017**, *195*, 247–256. [CrossRef]
4. Braun, J.; Saavedra Garcia, J.; Paniagua, G. Evaluation of the Unsteadiness Across Nozzles Downstream of Rotating Detonation Combustors. In *Proceedings of the 55th AIAA Aerospace Sciences Meeting, Grapevine, TX, USA, 9–13 January 2017*; American Institute of Aeronautics and Astronautics: Reston, VA, USA, 2017. [CrossRef]
5. Schwer, D.A.; Brophy, C.M.; Kelso, R.H. Pressure Characteristics of an Aerospike Nozzle in a Rotating Detonation Engine. In *Proceedings of the 2018 Joint Propulsion Conference, Cincinnati, OH, USA, 9–11 July 2018*; American Institute of Aeronautics and Astronautics: Reston, VA, USA, 2018. [CrossRef]

6. Bach, E.; Stathopoulos, P.; Paschereit, C.O.; Bohon, M.D. Performance Analysis of a Rotating Detonation Combustor Based on Stagnation Pressure Measurements. *Combust. Flame* **2020**, *217*, 21–36. [CrossRef]
7. Ruan, A.; Gejji, R.; Bach, E.; Slabaugh, C.D.; Paniagua, G. Effect of Geometric and Flow Parameters on a Hydrogen-Air Rotating Detonation Combustor Operability and Performance. In *Proceedings of the AIAA SCITECH 2025 Forum, Orlando, FL, USA, 6–10 January 2025*; American Institute of Aeronautics and Astronautics: Reston, VA, USA, 2025. [CrossRef]
8. Paniagua, G.; Iorio, M.; Vinha, N.; Sousa, J. Design and Analysis of Pioneering High Supersonic Axial Turbines. *Int. J. Mech. Sci.* **2014**, *89*, 65–77. [CrossRef]
9. Liu, Z.; Braun, J.; Paniagua, G. Characterization of a Supersonic Turbine Downstream of a Rotating Detonation Combustor. *J. Eng. Gas Turbines Power* **2018**, *141*, 031501 . [CrossRef]
10. Mushtaq, N.; Colella, G.; Gaetani, P. Design and Parametric Analysis of a Supersonic Turbine for Rotating Detonation Engine Applications. *Int. J. Turbomach. Propuls. Power* **2022**, *7*, 1. [CrossRef]
11. Liu, Z.; Braun, J.; Paniagua, G. Thermal Power Plant Upgrade via a Rotating Detonation Combustor and Retrofitted Turbine With Optimized Endwalls. *Int. J. Mech. Sci.* **2020**, *188*, 105918. [CrossRef]
12. Liu, Z.; Braun, J.; Paniagua, G. Performance of Axial Turbines Exposed to Large Fluctuations. In *Proceedings of the 53rd AIAA/SAE/ASEE Joint Propulsion Conference, Atlanta, GA, USA, 10–12 July 2017*; American Institute of Aeronautics and Astronautics: Reston, VA, USA, 2017. [CrossRef]
13. Liu, Z.; Braun, J.; Paniagua, G. Integration of a Transonic High-Pressure Turbine With a Rotating Detonation Combustor and a Diffuser. *Int. J. Turbo Jet-Engines* **2023**, *40*, 1–10. [CrossRef]
14. Grasa, S.; Paniagua, G. Design, Multi-Point Optimization, and Analysis of Diffusive Stator Vanes to Enable Turbine Integration Into Rotating Detonation Engines. *J. Turbomach.* **2024**, *146*, 111002. [CrossRef]
15. Grasa, S.; Paniagua, G. Design and Characterization of Highly Diffusive Turbine Vanes Suitable for Transonic Rotating Detonation Combustors. *Int. J. Turbomach. Propuls. Power* **2024**, *9*, 18. [CrossRef]
16. Gallis, P.; Salvadori, S.; Misul, D.A. Numerical Analysis of a Flow Control System for High-Pressure Turbine Vanes Subject to Highly Oscillating Inflow Conditions. *J. Turbomach.* **2025**, *147*, 121008. [CrossRef]
17. Nastasi, R.; Labrini, G.; Salvadori, S.; Misul, D.A. Shape Optimization of a Diffusive High-Pressure Turbine Vane Using Machine Learning Tools. *Energies* **2024**, *17*, 5642. [CrossRef]
18. Rose, M.G. Non-Axisymmetric Endwall Profiling in the HP NGV's of an Axial Flow Gas Turbine. In *Proceedings of the Volume 1: Turbomachinery, The Hague, The Netherlands, 13–16 June 1994*; GT1994; American Society of Mechanical Engineers: New York, NY, USA, 1994. [CrossRef]
19. Hartland, J.C.; Gregory-Smith, D.G.; Rose, M.G. Non-Axisymmetric Endwall Profiling in a Turbine Rotor Blade. In *Proceedings of the Volume 1: Turbomachinery, Stockholm, Sweden, 2–5 June 1998*; GT1998; American Society of Mechanical Engineers: New York, NY, USA, 1998. [CrossRef]
20. Hartland, J.C.; Gregory-Smith, D.G.; Harvey, N.W.; Rose, M.G. Non-Axisymmetric Turbine End Wall Design: Part II—Experimental Validation. In *Proceedings of the Volume 1: Aircraft Engine; Marine; Turbomachinery; Microturbines and Small Turbomachinery, Indianapolis, IN, USA, 7–10 June 1999*; GT1999; American Society of Mechanical Engineers: New York, NY, USA, 1999. [CrossRef]
21. Rose, M.G.; Harvey, N.W.; Seaman, P.; Newman, D.A.; McManus, D. Improving the Efficiency of the Trent 500 HP Turbine Using Non-Axisymmetric End Walls: Part II—Experimental Validation. In *Proceedings of the Volume 1: Aircraft Engine; Marine; Turbomachinery; Microturbines and Small Turbomachinery, New Orleans, LA, USA, 4–7 June 2001*; GT2001; American Society of Mechanical Engineers: New York, NY, USA, 2001. [CrossRef]
22. Praisner, T.J.; Allen-Bradley, E.; Grover, E.A.; Knezevici, D.C.; Sjolander, S.A. Application of Non-Axisymmetric Endwall Contouring to Conventional and High-Lift Turbine Airfoils. In *Proceedings of the Volume 6: Turbo Expo 2007, Parts A and B, Montreal, QC, Canada, 14–17 January 2007*; GT2007; American Society of Mechanical Engineers: New York, NY, USA, 2007. [CrossRef]
23. Turgut, Ö.H.; Camcı, C. A Nonaxisymmetric Endwall Design Approach and its Computational Assessment in the NGV of an HP Turbine Stage. *Aerosp. Sci. Technol.* **2015**, *47*, 456–466. [CrossRef]
24. Miyoshi, I.; Higuchi, S.; Kishibe, T. Improving the Performance of a High Pressure Gas Turbine Stage Using a Profiled Endwall. In *Proceedings of the Volume 6A: Turbomachinery, San Antonio, TX, USA, 3–7 June 2013*; GT2013; American Society of Mechanical Engineers: New York, NY, USA, 2013. [CrossRef]
25. Na, Z.; Liu, B. Numerical Investigation of Non-Axisymmetric Endwalls in a High Pressure Axial Flow Turbine. In *Proceedings of the Volume 2A: Turbomachinery, Montreal, QC, Canada, 15–19 June 2015*; GT2015; American Society of Mechanical Engineers: New York, NY, USA, 2015. [CrossRef]
26. Kim, I.; Kim, J.; Cho, J.; Kang, Y.S. Non-Axisymmetric Endwall Profile Optimization of a High-Pressure Transonic Turbine Using Approximation Model. In *Proceedings of the Volume 2B: Turbomachinery, Seoul, South Korea, 13–17 June 2016*; GT2016; American Society of Mechanical Engineers: New York, NY, USA, 2016. [CrossRef]

27. Snedden, G.; Dunn, D.; Ingram, G. On- and Off-Design Performance of a Model Rotating Turbine With Non-Axisymmetric Endwall Contouring and a Comparison to Cascade Data. *Aeronaut. J.* **2018**, *122*, 646–665. [CrossRef]
28. Dickel, J.A.; Marks, C.; Clark, J.; Sondergaard, R.; Wolff, M. Non-Axisymmetric Endwall Contouring of Front-Loaded High-Lift Low Pressure Turbines. In *Proceedings of the 2018 AIAA Aerospace Sciences Meeting, Kissimmee, FL, USA, 8–12 January 2018*; American Institute of Aeronautics and Astronautics: New York, NY, USA, 2018. [CrossRef]
29. Rehman, A.; Liu, B.; Song, Z. Design of Non-Axisymmetric Endwall of a Stator to Improve the Efficiency of a High-Pressure Turbine: A Pseudo Objective Function. In *Proceedings of the 13th European Conference on Turbomachinery Fluid Dynamics and Thermodynamics, Lausanne, Switzerland, 8–12 April 2019*; ETC13; European Turbomachinery Society: Florence, Italy, 2019. [CrossRef]
30. Rehman, A.; Liu, B. Numerical Investigation and Non-Axisymmetric Endwall Profiling of a Turbine Stage. *J. Therm. Sci.* **2019**, *28*, 811–825. [CrossRef]
31. Liu, W.; Wang, S.; Wen, F. Numerical Investigation of a Turbine Stator with Nonaxisymmetric Endwall Profiling. *J. Therm. Sci.* **2022**, *31*, 1790–1803. [CrossRef]
32. Burigana, M.; Verstraete, T.; Lavagnoli, S. Turbine Endwall Contouring Through Advanced Optimization Techniques. *J. Turbomach.* **2023**, *145*, 081011. [CrossRef]
33. Dènos, R.; Arts, T.; Paniagua, G.; Michelassi, V.; Martelli, F. Investigation of the Unsteady Rotor Aerodynamics in a Transonic Turbine Stage. *J. Turbomach.* **2000**, *123*, 81–89. [CrossRef]
34. Paniagua, G.; Dènos, R.; Almeida, S. Effect of the Hub Endwall Cavity Flow on the Flow-Field of a Transonic High-Pressure Turbine. *J. Turbomach.* **2004**, *126*, 578–586. [CrossRef]
35. Nacci, T.; Rosafio, N.; Salvadori, S.; Misul, D.; Paniagua, G. Analysis on the Effect of Cavity Flows on the Aerothermal Performance of a High-Pressure Turbine Stage. *J. Turbomach.* **2025**, *147*, 111010. [CrossRef]
36. Meng, L.; Zhang, X.; Yan, G.; Peng, C. Investigation of improving the hydraulic turbine cascade performance using non-axisymmetric endwall contouring. *Adv. Mech. Eng.* **2020**, *12*, 168781402091541. [CrossRef]
37. Niederreiter, H. Low-Discrepancy and Low-Dispersion Sequences. *J. Number Theory* **1988**, *30*, 51–70. [CrossRef]
38. Dalal, I.L.; Stefan, D.; Harwayne-Gidansky, J. Low-Discrepancy Sequences for Monte Carlo Simulations on Reconfigurable Platforms. In *Proceedings of the 2008 International Conference on Application-Specific Systems, Architectures and Processors*; IEEE: New York, NY, USA, 2008; pp. 108–113. [CrossRef]
39. ANSYS Inc. *Ansys Fluent Theory Guide*, 1st ed. ; ANSYS Inc.: Canonsburg, PA, USA, 2021.
40. Menter, F.R. Two-Equation Eddy-Viscosity Turbulence Models for Engineering Applications. *AIAA J.* **1994**, *32*, 1598–1605. [CrossRef] [PubMed]
41. Roache, P.J. Verification of Codes and Calculations. *AIAA J.* **1998**, *36*, 696–702. [CrossRef] [PubMed]
42. Aungier, R.H. *Turbine Aerodynamics: Axial-Flow and Radial-Flow Turbine Design and Analysis*; ASME Press: New York, NY, USA, 2006. [CrossRef]
43. ANSYS Inc. *DesignXplorer User's Guide*, 2nd ed.; ANSYS Inc.: Canonsburg, PA, USA, 2021.
44. Sieverding, C.H. Recent Progress in the Understanding of Basic Aspects of Secondary Flows in Turbine Blade Passages. *J. Eng. Gas Turbines Power* **1985**, *107*, 248–257. [CrossRef]